Robust Zeeman-type band splitting in sliding ferroelectrics

Homayoun Jafari,[1,*] Evgenii Barts,[1,*] Przemysław Przybysz,[1,2,*] Karma Tenzin,[1,3] Paweł J. Kowalczyk,[2] Paweł Dabrowski,[2] and Jagoda Sławińska[1,†]

[1]*Zernike Institute for Advanced Materials, University of Groningen, Nijenborgh 4, 9747 AG Groningen, The Netherlands*

[2]*Department of Solid State Physics, Faculty of Physics and Applied Informatics, University of Łódź, Pomorska 149/153, 90-236 Łódź, Poland*

[3]*Department of Physical Science, Sherubtse College, Royal University of Bhutan, 42007 Kanglung, Trashigang, Bhutan*

(Received 10 November 2023; accepted 29 January 2024; published 28 February 2024)

Transition metal dichalcogenides are known for their intriguing spin-valley effects, which can be harnessed through proximity in van der Waals heterostructures. Their hexagonal monolayers exhibit significant Zeeman band splitting of valence bands, reaching up to several hundred meV and giving rise to spin textures that yield long spin lifetimes. However, this effect is suppressed in the hexagonal bilayers due to inversion symmetry. The recent discovery of sliding ferroelectricity in MX_2 bilayers (M = Mo, W; X = S, Se) opens a pathway for the electrical control of the spin properties in these materials. While substantial Zeeman splitting is found in the rhombohedral structure, its behavior during the ferroelectric transition remains unclear. In this paper, we explore different stacking configurations of MX_2 bilayers by sliding and demonstrate, using density functional theory calculations and symmetry analysis, that the Zeeman effect completely dominates the spin polarization of bands throughout the structural transition. This promises to maintain robust spin transport in polar MX_2 bilayers, opening potential avenues for ferroelectric spintronics.

DOI: 10.1103/PhysRevMaterials.8.024005

I. INTRODUCTION

Two-dimensional (2D) transition metal dichalcogenides (TMDs) exhibit a variety of intriguing properties, such as tunable band gaps, high carrier mobilities, spin-valley locking, and strong light-matter interactions, making them ideal for exploring exotic fundamental phenomena and developing advanced electronic devices with enhanced functionalities. Recently, interfacial (or sliding) ferroelectricity was proposed in 2D materials [1,2], where the broken inversion symmetry induces an interlayer charge transfer and the electric polarization can be reversed by laterally sliding the layers by applying a vertical electric field [3]. This effect was initially observed in hexagonal boron nitride (h-BN) [4,5] and has been extended to rhombohedral-stacked (R-stacked) MX_2 (M = W, Mo; X = Se, S) homobilayers [6], MoS_2/WS_2 heterobilayers [7], and marginally twisted MoS_2 bilayers [8]. The combination of room-temperature ferroelectricity [9] and very low switching barriers (on the order of meV [3]) further enhances the potential applications of these atomically thin materials, making them suitable for ultrafast nonvolatile memories and optoelectronic devices. While the interplay between spin and polar degrees of freedom could bring additional functionalities [10–12], studies on band splitting, spin textures, or spin currents in ferroelectric TMDs are still limited [13,14].

The hexagonal monolayers of MX_2 with strong spin-orbit coupling (SOC) manifest the intriguing Zeeman band splitting locked at the K/K' valleys, which originates from the unique prismatic ligand coordination of the metal atom characteristic for TMDs. For heavy metal TMDs, the spin splitting of the valence band can reach up to several hundred meV, resulting in giant effective magnetic fields. Crucially, this band splitting and the associated out-of-plane spin texture can be transferred through proximity to other materials in van der Waals (vdW) heterostructures [15,16]. For instance, in graphene/TMD bilayers, the proximity-induced Zeeman effect enables the propagation of spins through the graphene layer despite its weak intrinsic SOC while also protecting out-of-plane spins against dephasing [17–19]. Thus, the Zeeman spin texture can be considered a persistent spin texture, ensuring robust spin transport in systems with broken inversion symmetry [20,21]. In contrast to monolayers, in H-stacked bilayers, the Zeeman band splitting is suppressed due to the presence of global inversion symmetry (IS) [22]. Although recent studies on R-stacked bilayers have revealed several noncentrosymmetric configurations with different symmetries that can be accessed through the lateral sliding mechanism [6,23,24], the potential presence of the Zeeman effect in these structures and its evolution upon sliding remain to be explored.

In this paper, we perform density functional theory (DFT) calculations for the family of sliding ferroelectrics MX_2 to unveil the link between the crystallographic point group symmetry, band splitting, and spin (orbital) texture of electronic states in the different regions of the Brillouin zone (BZ). We begin with an analysis of the ground state configuration described by the point group C_{3v} that exhibits a tiny out-of-plane electric polarization $P_\uparrow/P_\downarrow$ as confirmed by the experiments, and we show that regardless of the interplay of spin-orbit and layer coupling, a substantial Zeeman band spin is present

*These authors contributed equally to this work.
†Corresponding author: jagoda.slawinska@rug.nl

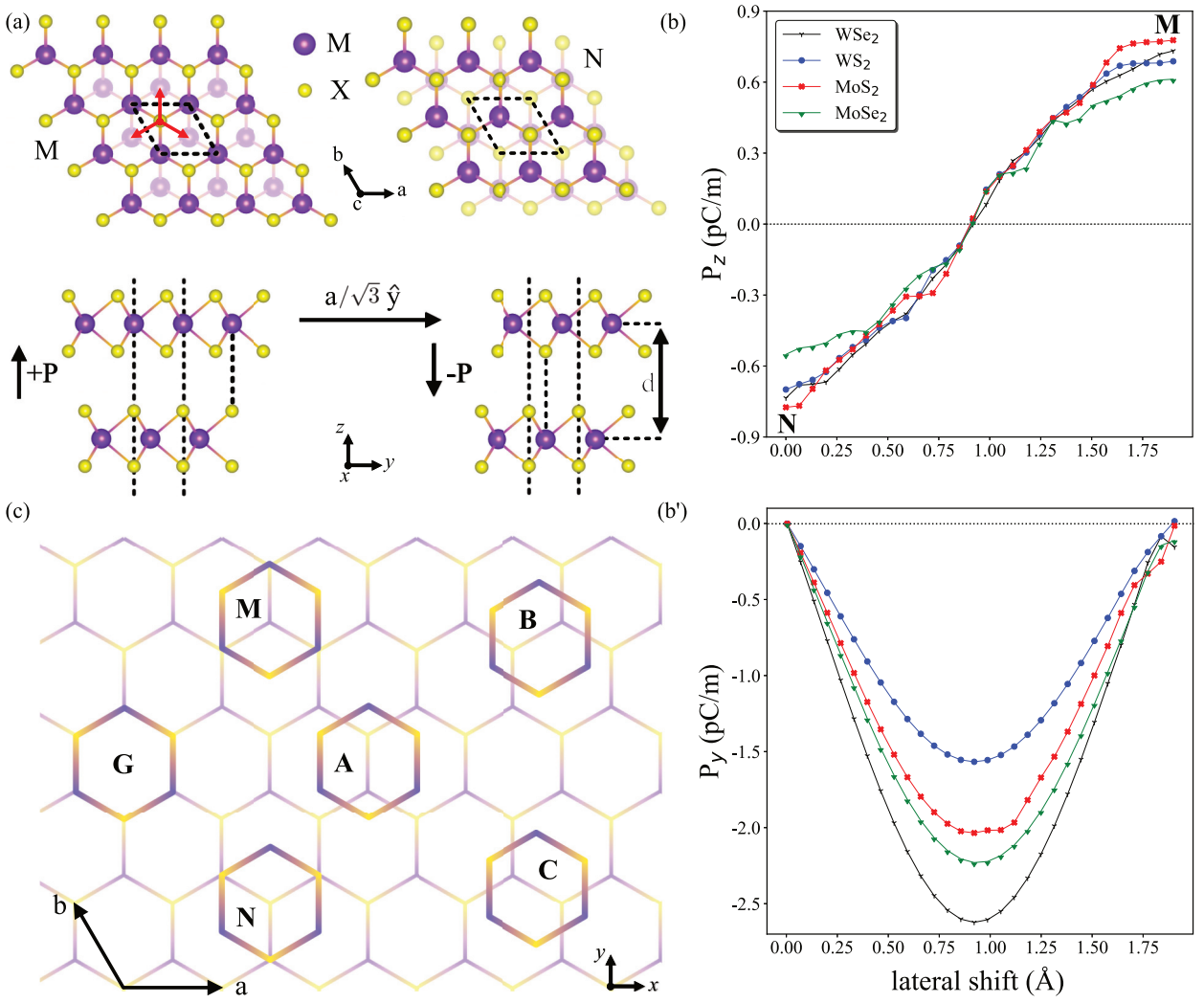

FIG. 1. (a) Crystal structure of an R-stacked MX_2 bilayer with polarization upwards ($P_\uparrow$) for **M** stacking and downwards ($P_\downarrow$) for **N** stacking. Top and side views are shown in the top and bottom panels, respectively. Black dashed lines denote the hexagonal unit cell. The red arrows show the three equivalent sliding directions. The interlayer distance d is indicated by the black arrow. (b) Out-of-plane electric polarization P_z versus lateral sliding between the **M** and **N** configurations calculated for all the considered compounds. The sliding path is along the [120] crystallographic direction (y axis). (b′) The same for the in-plane component P_y; $P_x = 0$ from symmetry. (c) Schematic view of different stacking configurations. The bottom layer is represented by the semitransparent honeycomb, and the different positions of the top layer are marked by single hexagons.

in the K/K' valleys, like in the case of monolayers. Further simulations of the lateral sliding between $P_\uparrow$ and $P_\downarrow$ configurations reveal that a decrease in the out-of-plane polarization is accompanied by the emergence of the in-plane component $P_\rightarrow$, which is parallel to the sliding direction, as determined by the C_s symmetry of the stackings along the sliding path [24]. Notably, $P_\rightarrow$ is larger than $P_\uparrow/P_\downarrow$ and achieves the largest value at the midpoint of the transition path, where the out-of-plane component is forbidden by the C_{2v} symmetry. In this intermediate state, which is not paraelectric, the Zeeman band splitting survives and extends to nearly the entire BZ. Our symmetry analysis reveals that the persistent Zeeman effect dictates the spin texture in all stacking configurations accessible via sliding due to the symmetry of the little point group at the corners of the BZ and the strong polarity of the prismatic coordination, which cannot easily be suppressed in the absence of IS.

II. STRUCTURE AND FERROELECTRICITY

TMDs possess multiple crystallographic phases with unique properties determined by the symmetries. Some of these properties also critically depend on the stacking order, such as the evolution of ferroelectricity when adjacent layers are laterally shifted with respect to each other. In contrast to centrosymmetric H-stacked bilayers, the layers in R-stacked configurations are oriented parallel to each other without any relative rotation [23,25]. As shown in Fig. 1(a), the top layer's metal ions align directly above the bottom layer's chalcogen ions, and chalcogen ions lie above the centers of the hexagonal rings in the **M** stacking or vice versa, with chalcogen atoms placed above the metal ions in the **N** stacking. Both configurations exhibit out-of-plane electric polarization P_z, either positive or negative, arising from the electrostatic potential drop between the layers due to the asymmetric charge

TABLE I. Different band parameters defined in Fig. 2 calculated for all considered materials. $E_{K\Gamma}$ is the difference between the topmost valence band energies at the Γ and K points, α_R is the Rashba parameter, $\Delta^{\Gamma}_{\text{layer}}$ is the layer splitting at Γ, Δ^{K}_{spin} is the spin splitting at K, and $\Delta^{K}_{\text{layer}}$ is the layer splitting at the K point. P_z denotes the out-of-plane component of the electric polarization. NG means negligible values that are beyond the accuracy of our calculations.

	MoS_2	$MoSe_2$	WS_2	WSe_2
$E_{K\Gamma} = E(K) - E(\Gamma)$ (meV)	−344	12	−108	138
$\alpha_R = 2E_R/k_R$ (eV Å)	NG	0.015	NG	0.012
$\Delta^{\Gamma}_{\text{layer}} = E^{\Gamma}_{\text{T}} - E^{\Gamma}_{\text{B}}$ (meV)	693	592	659	633
$\Delta^{K}_{\text{spin}} = E^{K}_{\text{S}\downarrow} - E^{K}_{\text{S}\uparrow}$ (meV)	148	184	417	453
$\Delta^{K}_{\text{layer}} = E^{K}_{\text{T}} - E^{K}_{\text{B}}$ (meV)	60	43	57	60
P_z (pC/m)	0.77	0.59	0.69	0.73
Total band gap (eV)	1.273	1.265	1.341	1.087

distribution at the interface [1,6]. The ferroelectric transition that corresponds to the switching between **M** and **N** stacking orders can be realized by laterally sliding the top layer along one of the three equivalent paths depicted by the three red arrows. For our first-principles simulations, we have chosen the path along the [120] direction (y axis) and calculated the electric polarization for intermediate phases between the **M** and **N** configurations (see Sec. VI for details). The values of P_z with respect to the lateral shift are plotted in Fig. 1(b). While the maximal magnitudes are below 1 pC/m, in agreement with previous calculations [1], MSe_2 and MS_2 exhibit the smallest and largest values, respectively (see Table I). The full transition path between the maximal and minimal P_z requires a sliding distance equal to $a/\sqrt{3}$ that corresponds to approximately 1.8–1.9 Å. We note that at the midpoint, the out-of-plane polarization vanishes, resembling a paraelectric state.

However, recent research by Ji *et al.* revealed that the polarization landscape in sliding ferroelectrics is more intricate than previously thought, indicating that in-plane components are allowed by symmetry for most of the parallel stacking configurations [24]. Indeed, our calculations have shown in-plane components that emerge along the transition path. Figure 1(b′) shows P_y components calculated for the atomic configurations from Fig. 1(b); P_x components turn out to be negligible. For **M** and **N** stacking orders, the values of P_y are zero, and they gradually increase when going towards the midpoint **A**. Remarkably, the in-plane components reach between 1.5 and 2.5 pC/m, exceeding the values of P_z. The evolution of P_y is quite similar to that of h-BN [24,26]. The possibility of electrically controlling in-plane electric polarization in vdW bilayers still needs to be experimentally verified.

The allowed direction of $\vec{P}$ can be determined based on the crystallographic point group [24], but the crystal symmetries are also essential for understanding the spin polarization of bands. We will thus start by analyzing the symmetries of the most relevant stacking orders. To provide a clear visual representation of different phases and their point group symmetries, we schematically depict them in Fig. 1(c). The bottom layer is shown as a semitransparent honeycomb lattice, while the individual hexagons on top of it correspond to different relative shifts of the top layer. Following the convention from Ref. [24], the fully parallel stacking denoted as **G** can be characterized by the lateral shift of the top layer relative to the bottom one, parametrized as (0,0) within the basis of the lattice vectors $\vec{a}$ and $\vec{b}$. Similarly, the configurations **M** and **N** can be generated by vectors $(\frac{1}{3}, \frac{2}{3})$ and $(\frac{2}{3}, \frac{1}{3})$, respectively. The stacking orders corresponding to the midpoints along the three equivalent sliding paths are denoted as **A**, **B**, and **C** and are obtained via shifts by vectors $(\frac{1}{2}, 0)$, $(0, \frac{1}{2})$, and $(\frac{1}{2}, \frac{1}{2})$, respectively.

In each of these phases, specific symmetries prohibit some components of the polarization vector. For example, stacking **G** is described by the point group D_{3h} generated by the improper rotation S_3 around the z axis and the mirror plane m_z. Like in the case of monolayers belonging to the same point group, the electric polarization is entirely prohibited by the presence of improper rotation. The stacking orders **M** and **N** are characterized by the point group C_{3v} with the threefold rotation 3_z and three mirror planes parallel to the rotation axis. These symmetries allow only for out-of-plane electric polarization, as confirmed by first-principles and experimental studies. The sliding between the **M** and **N** configurations reduces the symmetry of intermediate phases to C_s with only one mirror plane that is parallel to the sliding direction and perpendicular to the layers. In this case, group theory calculations predict both out-of-plane and in-plane components of electric polarization with the latter parallel to the sliding direction for any of the three equivalent paths [24]. This is consistent with our results that show the presence of the P_z and P_y components upon sliding along the y axis, as P_x components are forbidden by the mirror reflection m_y. Finally, the midpoints **A**, **B**, and **C** have the symmetry C_{2v}, which allows only the in-plane polarization, again in agreement with our calculations.

III. ELECTRONIC PROPERTIES OF M- AND N-STACKED BILAYERS

We will start with the discussion of the ground state configurations **M** and **N** with purely out-of-plane electric polarization enforced by the crystallographic point group C_{3v}. Based on our first-principles electronic structures summarized in Fig. 2, all crystals possess indirect energy gaps, with the conduction band minimum along the K-Γ line and the valence band maximum located either at Γ or at the K/K' points for sulfides and selenides, respectively. Apart from the band gaps, the electronic structures are characterized by various parameters, such as band splittings and band-edge energy offsets, defined in Fig. 2. Their magnitudes calculated for all four crystals are summarized in Table I.

The electronic states exhibit two types of band splitting: one originating from SOC and the other originating from layer coupling [27]. This double splitting is the most visible around K/K' [Fig. 2(e)], where the electron states can be described by a minimal Hamiltonian:

$$H_K = -\frac{\Delta_{\text{spin}}}{2}\sigma_z - \frac{\Delta_{\text{layer}}}{2}\tau_z, \tag{1}$$

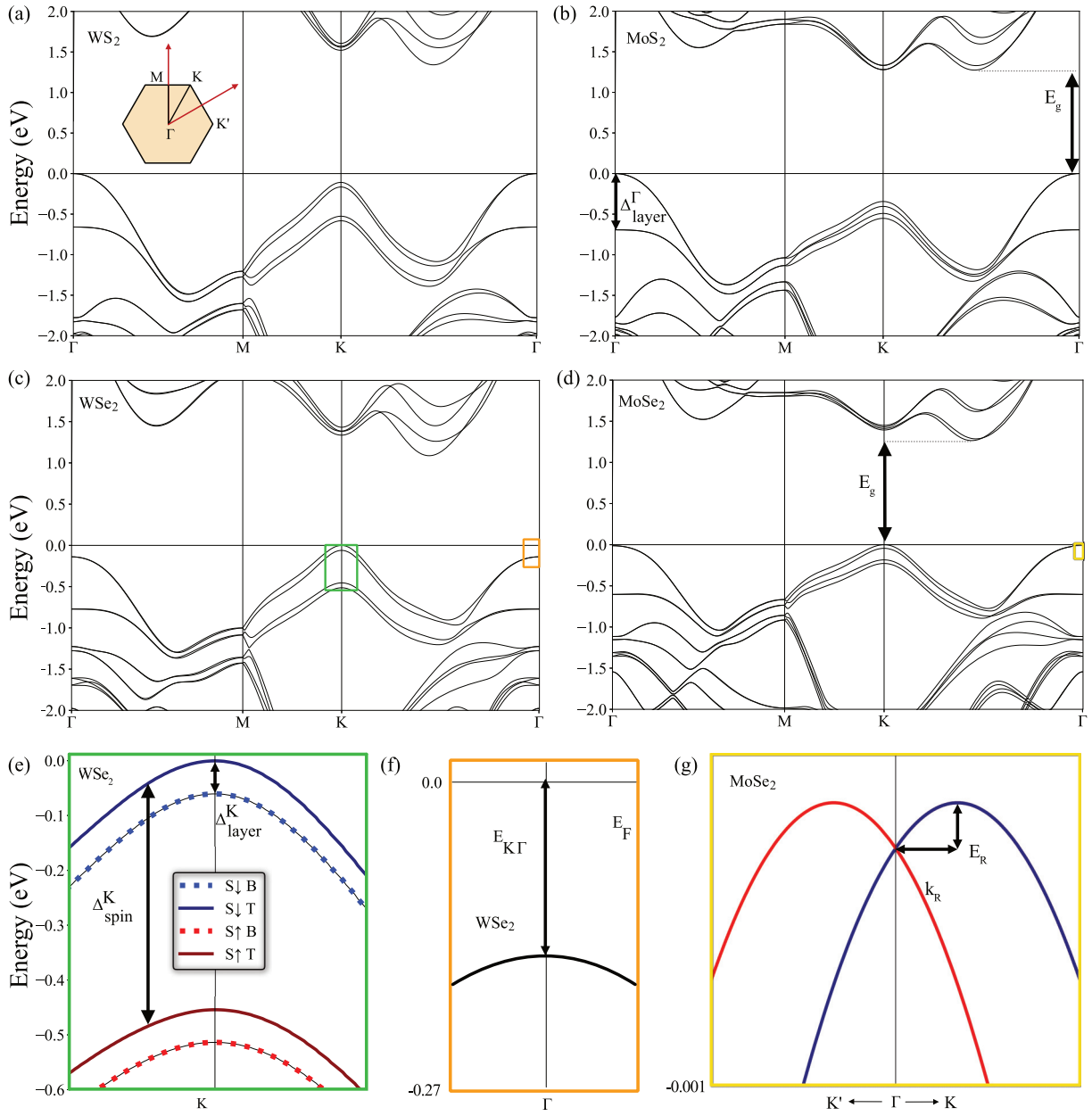

FIG. 2. (a)–(d) Band structures of **M** and **N** stacking configurations calculated for different MX_2. The inset shows the Brillouin zone (BZ) and the high-symmetry lines. The arrows indicate the band parameters: indirect energy gaps E_g and layer splitting at the Γ point $\Delta^{\Gamma}_{\text{layer}}$. (e) A zoom of the electronic structure around the K point marked by the green rectangle in (c). The colors denote out-of-plane spin polarization originating from the Zeeman interaction, and the solid and dashed lines represent the top and bottom layers, respectively. The spin splitting (Δ^{K}_{spin}) and layer splitting ($\Delta^{K}_{\text{layer}}$) parameters are indicated by the arrows. (f) A zoom of the electronic structure around the Γ point marked by the orange rectangle in (c). $E_{K\Gamma}$ denotes the offset between the valence band edge at the K and Γ points. (g) A zoom of the electronic structure around the Γ point marked by the yellow rectangle in (d). The colored lines represent the spin texture perpendicular to the momentum, indicating a purely Rashba spin texture with the Rashba coefficient defined as $\alpha_R = 2E_R/k_R$. The numerical values of all the parameters are listed in Table I.

with σ_z and τ_z denoting Pauli matrices in the spin and layer spaces, respectively. The first term represents the Dirac mass term, acting as an effective intrinsic magnetic field and causing Zeeman spin splitting with an energy gap Δ_{spin}. For the K (K') valley, the value of Δ_{spin} is positive (negative) due to time-reversal symmetry, which flips the spin polarization from the K to $-K$ point. This splitting reaches several hundred meV (see Table I), which is similar to that of monolayers [28,29]. The second term accounts for band energy splitting due to layer coupling, with Δ_{layer} ranging from 50 meV at the K/K' point to 600 meV at the Γ point (the evolution of the layer splitting along high-symmetry lines is shown in Fig. S1 in the Supplemental Material [30]).

To understand the spin-momentum coupling observed at the Γ and K points, we conducted a symmetry analysis based on group theory. At the Γ point, the symmetry is described by

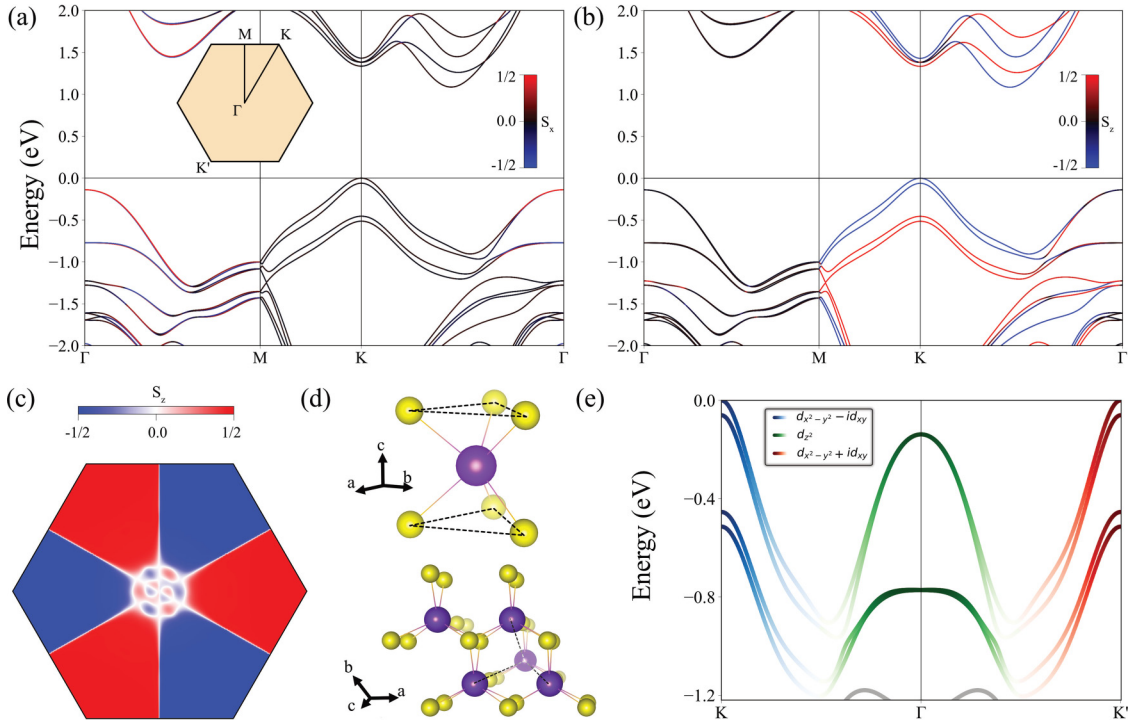

FIG. 3. (a) and (b) Spin-resolved band structure of **N**-stacked WSe_2. (a) shows the S_x component of the spin texture; S_y is omitted, as it emerges only along the Γ-K line close to the BZ center. (b) shows the out-of-plane component S_z. (c) S_z component calculated for the topmost valence band in the entire BZ. (d) Illustration of trigonal prismatic ligand coordination in hexagonal MX_2; top and side views are displayed in the top and bottom panels. The dashed lines represent the connection between the ligands and metal atoms located in different layers. (e) Orbital-resolved band structure of WSe_2 along K-Γ-K'. For the sake of completeness, the layer-resolved bands are additionally shown in Fig. S1 in the Supplemental Material [30].

the small group $C_{3v} = \{3_z, m_x\}$, which consists of a threefold rotational symmetry axis 3_z and a vertical mirror symmetry plane m_x, allowing only Rashba-type spin-momentum coupling [31]:

$$\alpha_R(k_x\sigma_y - k_y\sigma_x). \tag{2}$$

By using one-dimensional complex representations of 3_z, wherein the coordinates (x, y) transform as

$$3_z \cdot (r_+, r_-, z) = (e^{-i2\pi/3}r_+, e^{i2\pi/3}r_-, z), \tag{3}$$

with $r_\pm = x \pm iy$, we obtain two invariant combinations: $r_+\sigma_-$ and $r_-\sigma_+$. Their sum leads to Eq. (2), and their difference is a Weyl-type coupling: $\alpha_W(k_x\sigma_x + k_y\sigma_y)$, which is, however, prohibited by the mirror symmetry $m_x \cdot (x, y, z) = (-x, y, z)$. The purely Rashba spin textures are confirmed by our first-principles calculations [see $MoSe_2$ in Fig. 2(g)], although the corresponding splittings are tiny for all considered materials (see Table I).

The spin-momentum coupling at the K/K' points is governed by the small symmetry group $C_3 = \{3_z\}$; hence, both Rashba- and Weyl-type spin textures are permitted. However, our DFT results show that the dominant spin anisotropic interaction in the large k area is the Zeeman splitting, which surpasses the Rashba and Weyl interactions, resulting in a significant band splitting with strongly out-of-plane-polarized spin textures [see Fig. 3(a)–3(c)]. This agrees with 3_z symmetry, which allows for a nonzero spin polarization at the K point [32] but restricts zero in-plane components for a nondegenerate band ψ_K, $\langle\sigma_{x,y}\rangle = 0$, since $\langle\psi_K|3_z^{-1}\sigma_\pm 3_z|\psi_K\rangle = e^{\pm i2\pi/3}\langle\psi_K|\sigma_\pm|\psi_K\rangle = 0$. Remarkably, the transition between Zeeman and Rashba spin textures occurs as an abrupt band inversion that interchanges the layer and spin splitting quite close to the Γ point [see Fig. 3(b)], in contrast to the rather smooth decrease of spin splitting along the K-Γ path found in monolayer TMDs.

The out-of-plane spin polarization at the K point is permitted by symmetry, but the explanation for the giant splitting requires further analysis. We argue that the large Zeeman interaction stems from a sizable orbital momentum, characteristic of the strongly polar prismatic ligand ion coordination of transition metals in TMDs, as schematically illustrated in Fig. 3(d). The prismatic crystal field splits the d orbitals of W (Mo) into three configurations: $\{d_{xy}, d_{x^2-y^2}\}$, $\{d_{3z^2-r^2}\}$, and $\{d_{xz}, d_{yz}\}$. In all the compounds, the valence band states are predominantly composed of the d_{xy} and $d_{x^2-y^2}$ orbitals, specifically $d_{x^2-y^2} - id_{xy}$ and $d_{x^2-y^2} + id_{xy}$ at the K and K' points, respectively [28,33]. Figure 3(e) shows the orbital-resolved band structure calculated for WSe_2, confirming our analysis. We note that these states are eigenstates of the L_z projection of atomic orbital momentum:

$$L_z(|d_{x^2-y^2}\rangle \pm i|d_{xy}\rangle) = \pm 2(|d_{x^2-y^2}\rangle \pm i|d_{xy}\rangle), \tag{4}$$

which can be deduced using the real-space representation of $L_z = -i(x\frac{\partial}{\partial y} - y\frac{\partial}{\partial x})$, where the $|d_{x^2-y^2}\rangle \pm i|d_{xy}\rangle$ state transforms as the $x^2 - y^2 \pm i2xy$ function. Consequently, the relatively large Zeeman interaction at the K point originates directly from the SOC: $\lambda(\boldsymbol{L}\cdot\boldsymbol{S}) = -2\lambda S_z$, where $S_z = \sigma_z/2$. Here, we use the fact that the expectation values of the x and

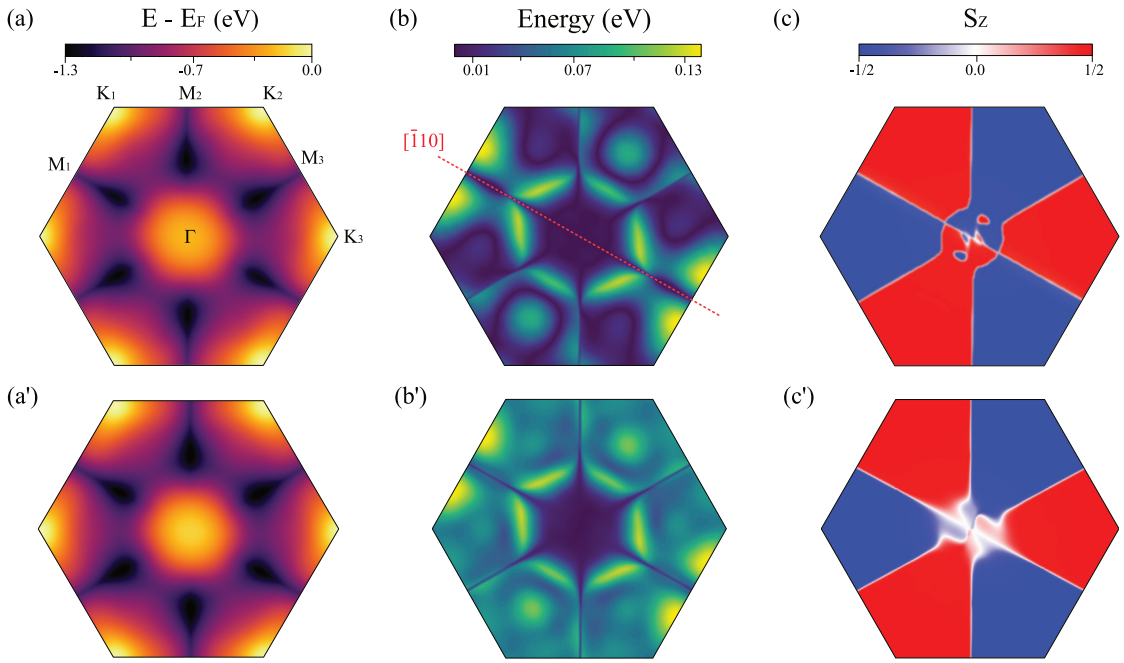

FIG. 4. (a) Energy of the topmost valence band calculated over the entire BZ for the intermediate state (**A**) of WSe_2. The bright spots at the corners of the BZ represent the valence band maximum. The labels indicate the high-symmetry points. The energy splitting and spin polarization of this band are shown in (b) and (c). The dashed line represents the [$\bar{1}$10] crystallographic direction defined in the reciprocal lattice. In (c), only the S_z component of the spin texture is shown, as S_x and S_y are nearly negligible and are present only in the close vicinity of Γ. Analogous data are reported for the rest of considered materials in Fig. S2 in the Supplemental Material [30]. (a′)–(c′) The same as (a)–(c), but calculated for the stacking configuration between the **N** and **A** points.

y orbital momentum components are zero within the d_{xy} and $d_{x^2-y^2}$ orbital manifolds, as also dictated by the 3_z symmetry. Analogous arguments apply to monolayer TMDs [22,28].

IV. ELECTRONIC PROPERTIES OF THE INTERMEDIATE STATES

We will now focus on the electronic structure and spin texture of the intermediate state **A** shown schematically in Fig. 1(c). This bilayer possesses mirror symmetry m_y along the sliding direction, a glide mirror $\overline{m}_z$ consisting of a mirror plane parallel to the layers and fractional translation along the x direction, and screw symmetry with the twofold rotation 2_y followed by translation along the x axis. Although the C_{2v} symmetry results in an orthorhombic structure, we opted to use a hexagonal unit cell for calculations, similar to the **M** and **N** stacking configurations. However, it is important to note that the absence of threefold symmetry in the intermediate state leads to different high-symmetry points in the BZ. Thus, to better visualize the symmetries, we provide maps of the properties of the topmost valence band throughout the full BZ, rather than standard band structures along high-symmetry lines. The results of calculations performed for WSe_2 are summarized in Figs. 4(a)–4(c).

Figure 4(a) displays the energy map of the topmost valence band. Although it may initially appear to exhibit threefold symmetry, a closer examination of the band shape around the BZ center reveals a distortion along the [$\bar{1}$10] direction in the reciprocal lattice. This anisotropy is even more evident in the map of band splitting shown in Fig. 4(b), which shows a clear twofold pattern. We find that different corners of the BZ exhibit distinct electronic structures, in contrast to the **M** and **N** configurations. For instance, we observe two different K and M points with the band splitting along K_1-M_1 approximately 100 meV larger than that along K_2-M_2. Surprisingly, the S_z component of the spin texture, plotted in Fig. 4(c), reveals nearly perfect threefold symmetry similar to the C_{3v} configurations [compare with Fig. 3(c)], except for a tiny region close to Γ. Notably, the S_z component of the spin texture is now prevalent throughout the entire BZ. This can be rationalized by the mirror symmetry $\overline{m}_z$ that now belongs to the symmetry group of an arbitrary point in the BZ and does not allow an in-plane spin projection. Additionally, linear spin-momentum coupling at the Γ point in the BZ is prohibited by $\overline{m}_z$.

It is worth noting that other stacking configurations along the sliding path display similar Zeeman-type band splitting in the major part of the BZ. For example, Figs. 4(a′)–4(c′) summarize the properties of the topmost valence band of WSe_2 in the stacking configuration intermediate between the **N** and **A** points, which is described by point group C_s. Not surprisingly, the S_z component of the spin texture shows differences when compared to **N** and **A** only in the close vicinity of the Γ point. In fact, the spin pattern around the center of the BZ resembles the **N/M** configurations, albeit without the threefold symmetry present in the latter [see Fig. 3(c)]. Therefore, we can conclude that Zeeman spin texture is extremely robust and cannot be eliminated via sliding. We observed the same trends for all the considered compounds (see the Supplemental Material [30]).

V. CONCLUSIONS

In summary, we explored different noncentrosymmetric stacking orders of MX_2 bilayers using first-principles calculations and symmetry analysis. We focused first on the behavior of electric polarization upon sliding between two configurations with purely out-of-plane electric dipoles, commonly associated with sliding ferroelectricity. Remarkably, our findings revealed the emergence of in-plane polarization components parallel to the sliding direction, in addition to the perpendicular components, that reach their maximum values at the midpoint of the transition path. The nonzero electric polarization suggests that the intermediate state is neither centrosymmetric nor paraelectric.

Furthermore, the same crystal symmetries that determine the direction of electric polarization also significantly impact the electronic states, particularly the spin texture. In R-stacked bilayers, the band structures exhibit two distinct types of splitting: one originating from SOC and the other originating from layer coupling. Around the two valleys, the dominant feature is the Zeeman band splitting, reaching magnitudes of several hundreds of meV. This giant splitting is enabled by the symmetries arising from the prismatic ligand coordination of the metal atoms, which dictate the configuration of the valence states and lead to substantial spin splitting arising directly from SOC, similar to the case of monolayers. Additionally, consistent with time-reversal symmetry, opposite spin moments are observed in the two valleys, K and $-K$. An extra splitting of each of these spin-split bands occurs due to layer coupling, but it becomes dominant only in the vicinity of the Γ point.

In addition, we studied spin polarization of the intermediate states along the transition path. The midpoint configuration, characterized by the point group C_{2v}, exhibits an enhanced Zeeman-type persistent spin texture that now extends throughout nearly the entire BZ. This behavior is attributed to the presence of glide reflection $\overline{m}_z$, which prevents in-plane spin projection at any point in the reciprocal lattice. While larger regions display the Zeeman band splitting, the change from threefold to twofold symmetry does not significantly alter the arrangement of spin texture in the BZ. Interestingly, other stacking configurations accessible through sliding, such as those described by point groups C_s and C_2, exhibit similar Zeeman splitting resembling either the C_{3v} or C_{2v} symmetry configurations. The only way to eliminate this splitting is either to restore the global inversion symmetry or to twist the layers to modify the little group of different points in the BZ.

In terms of spin transport, any of the considered bilayers can serve a role similar to that of monolayers, effectively protecting propagating spins from randomization during scattering. Additionally, by populating one of the valleys, additional phenomena like the valley Hall effect can be achieved [34–36]. Breaking time-reversal symmetry can be accomplished through the application of electric or magnetic fields or via circularly polarized optical excitation [37,38]. Furthermore, unlike monolayers, the studied structures exhibit sliding ferroelectricity and a complex polarization landscape, offering numerous opportunities for further exploration that include multistate ferroelectricity and moiré domains in twisted structures [8,39,40]. The combination of these peculiar ferroelectric properties at room temperature, along with robust spin transport, opens up intriguing possibilities for electronic devices endowed with enhanced functionalities.

TABLE II. Structural parameters of all considered crystals; a, $d_{\mathrm{M-X}}$, $d_{\mathrm{X-X}}$, $\delta_{\mathrm{X-M-X}}$, and d denote lattice constants, bond lengths M-X and X-X, the bond angle between X-M-X, and the interlayer distance, respectively.

	MoS_2	$MoSe_2$	WS_2	WSe_2
a (Å)	3.16	3.28	3.15	3.28
$d_{\mathrm{M-X}}$ (Å)	2.40	2.53	2.40	2.53
$d_{\mathrm{X-X}}$ (Å)	3.13	3.53	3.15	3.37
$\delta_{\mathrm{X-M-X}}$ (deg)	81.34	82.90	81.83	83.29
d (Å)	6.16	6.62	6.23	6.53

VI. METHODS

Our first-principles calculations were performed using the QUANTUM ESPRESSO [41,42] simulation package. The electron-ion interactions were described via the projector augmented wave method [43,44], and the wave functions were expanded in a plane wave basis set with a cutoff of 800 eV. Based on the experimental structure parameters of bulk MX_2 [23], we constructed slabs consisting of two MX_2 layers. A vacuum region of 20 Å along the c axis was used to separate the spurious images of bilayers to minimize their interactions. The internal degrees of freedom were further relaxed until the forces were below 10^{-3} Ry bohr^{-1}, employing the Perdew-Burke-Ernzerhof parametrization of generalized gradient approximation and vdW corrections (DFT-D3) [45]. The BZ is sampled on k meshes of $12\times12\times1$. The optimized structural parameters are given in Table II. The electric polarization was calculated using the Berry phase approach implemented in QUANTUM ESPRESSO. However, it is important to mention that the accurate procedure requires the calculation of the centrosymmetric phase, which is not applicable in the case of parallel-stacked MX_2 bilayers. To obtain the values of P_z and P_y, we subtracted the values P_z^0 and P_y^0 calculated in the stacking configurations, where these components, instead of the full polarization vector, should vanish by symmetry. The electric polarization was calculated for 20 configurations along the path connecting two ferroelectric ground states **N** and **M**. Spin-orbit coupling was taken into account self-consistently in all the simulations except for the relaxations and Berry phase calculations. The postprocessing calculations of the band structures and spin textures on dense k meshes were performed using the PAOFLOW code [46,47].

All data associated with the results reported in this paper are available from DataverseNL [48].

ACKNOWLEDGMENTS

We thank B. van Dijk for his helpful contribution. J.S. acknowledges the Rosalind Franklin Fellowship from the

University of Groningen. J.S. and E.B. acknowledge the funding from NWO under Contract No. NWA.1418.22.014. Part of this work was supported by the National Science Centre, Poland, under Grant No. 2018/30/E/ST5/00667. The calculations were carried out on the Dutch national e-infrastructure with the support of SURF Cooperative (EINF-5312) and on the Hábrók high-performance computing cluster of the University of Groningen.

[1] L. Li and M. Wu, Binary compound bilayer and multilayer with vertical polarizations: Two-dimensional ferroelectrics, multiferroics, and nanogenerators, ACS Nano **11**, 6382 (2017).

[2] J. Park, I. W. Yeu, G. Han, C. S. Hwang, and J.-H. Choi, Ferroelectric switching in bilayer 3R MoS_2 via interlayer shear mode driven by nonlinear phononics, Sci. Rep. **9**, 14919 (2019).

[3] M. Wu and J. Li, Sliding ferroelectricity in 2D van der Waals materials: Related physics and future opportunities, Proc. Natl. Acad. Sci. USA **118**, e2115703118 (2021).

[4] M. Vizner Stern, Y. Waschitz, W. Cao, I. Nevo, K. Watanabe, T. Taniguchi, E. Sela, M. Urbakh, O. Hod, and M. Ben Shalom, Interfacial ferroelectricity by van der Waals sliding, Science **372**, 1462 (2021).

[5] K. Yasuda, X. Wang, K. Watanabe, T. Taniguchi, and P. Jarillo-Herrero, Stacking-engineered ferroelectricity in bilayer boron nitride, Science **372**, 1458 (2021).

[6] X. Wang, K. Yasuda, Y. Zhang, S. Liu, K. Watanabe, T. Taniguchi, J. Hone, L. Fu, and P. Jarillo-Herrero, Interfacial ferroelectricity in rhombohedral-stacked bilayer transition metal dichalcogenides, Nat. Nanotechnol. **17**, 367 (2022).

[7] L. Rogée, L. Wang, Y. Zhang, S. Cai, P. Wang, M. Chhowalla, W. Ji, and S. P. Lau, Ferroelectricity in untwisted heterobilayers of transition metal dichalcogenides, Science **376**, 973 (2022).

[8] A. Weston *et al.*, Interfacial ferroelectricity in marginally twisted 2D semiconductors, Nat. Nanotechnol. **17**, 390 (2022).

[9] Y. Liu, S. Liu, B. Li, W. J. Yoo, and J. Hone, Identifying the transition order in an artificial ferroelectric van der Waals heterostructure, Nano Lett. **22**, 1265 (2022).

[10] S. Manipatruni, D. E. Nikonov, C.-C. Lin, T. A. Gosavi, H. Liu, B. Prasad, Y.-L. Huang, E. Bonturim, R. Ramesh, and I. A. Young, Scalable energy-efficient magnetoelectric spin–orbit logic, Nature (London) **565**, 35 (2019).

[11] P. Noël *et al.*, Non-volatile electric control of spin–charge conversion in a $SrTio_3$ Rashba system, Nature (London) **580**, 483 (2020).

[12] S. Varotto *et al.*, Room-temperature ferroelectric switching of spin-to-charge conversion in germanium telluride, Nat. Electron. **4**, 740 (2021).

[13] Z. Lin, C. Si, S. Duan, C. Wang, and W. Duan, Rashba splitting in bilayer transition metal dichalcogenides controlled by electronic ferroelectricity, Phys. Rev. B **100**, 155408 (2019).

[14] H. Jafari, A. Roy, and J. Sławińska, Ferroelectric control of charge-to-spin conversion in WTe_2, Phys. Rev. Mater. **6**, L091404 (2022).

[15] W. Yan, O. Txoperena, R. Llopis, H. Dery, L. E. Hueso, and F. Casanova, A two-dimensional spin field-effect switch, Nat. Commun. **7**, 13372 (2016).

[16] J. H. Garcia, M. Vila, A. W. Cummings, and S. Roche, Spin transport in graphene/transition metal dichalcogenide heterostructures, Chem. Soc. Rev. **47**, 3359 (2018).

[17] T. S. Ghiasi, J. Ingla-Aynés, A. A. Kaverzin, and B. J. Van Wees, Large proximity-induced spin lifetime anisotropy in transition-metal dichalcogenide/graphene heterostructures, Nano Lett. **17**, 7528 (2017).

[18] L. A. Benítez, J. F. Sierra, W. Savero Torres, A. Arrighi, F. Bonell, M. V. Costache, and S. O. Valenzuela, Strongly anisotropic spin relaxation in graphene–transition metal dichalcogenide heterostructures at room temperature, Nat. Phys. **14**, 303 (2018).

[19] J. Ingla-Aynés, F. Herling, J. Fabian, L. E. Hueso, and F. Casanova, Electrical control of valley Zeeman spin-orbit-coupling–induced spin precession at room temperature, Phys. Rev. Lett. **127**, 047202 (2021).

[20] L. Tao and E. Y. Tsymbal, Perspectives of spin-textured ferroelectrics, J. Phys. D **54**, 113001 (2021).

[21] J. Sławińska, F. T. Cerasoli, P. Gopal, M. Costa, S. Curtarolo, and M. Buongiorno Nardelli, Ultrathin SnTe films as a route towards all-in-one spintronics devices, 2D Mater. **7**, 025026 (2020).

[22] H. Yuan, M. S. Bahramy, K. Morimoto, S. Wu, K. Nomura, B.-J. Yang, H. Shimotani, R. Suzuki, M. Toh, C. Kloc, X. Xu, R. Arita, N. Nagaosa, and Y. Iwasa, Zeeman-type spin splitting controlled by an electric field, Nat. Phys. **9**, 563 (2013).

[23] J. He, K. Hummer, and C. Franchini, Stacking effects on the electronic and optical properties of bilayer transition metal dichalcogenides MoS_2, $MoSe_2$, WS_2, and WSe_2, Phys. Rev. B **89**, 075409 (2014).

[24] J. Ji, G. Yu, C. Xu, and H. J. Xiang, General theory for bilayer stacking ferroelectricity, Phys. Rev. Lett. **130**, 146801 (2023).

[25] Z. Li, J. Förste, K. Watanabe, T. Taniguchi, B. Urbaszek, A. S. Baimuratov, I. C. Gerber, A. Högele, and I. Bilgin, Stacking-dependent exciton multiplicity in WSe_2 bilayers, Phys. Rev. B **106**, 045411 (2022).

[26] D. Bennett, G. Chaudhary, R.-J. Slager, E. Bousquet, and P. Ghosez, Polar meron-antimeron networks in strained and twisted bilayers, Nat. Commun. **14**, 1629 (2023).

[27] L. M. Schneider, J. Kuhnert, S. Schmitt, W. Heimbrodt, U. Huttner, L. Meckbach, T. Stroucken, S. W. Koch, S. Fu, X. Wang, K. Kang, E.-H. Yang, and A. Rahimi-Iman, Spin-layer and spin-valley locking in CVD-grown AA′ and AB-stacked tungsten disulfide bilayers, J. Phys. Chem. C **123**, 21813 (2019).

[28] S. Bhowal and S. Satpathy, Intrinsic orbital and spin Hall effects in monolayer transition metal dichalcogenides, Phys. Rev. B **102**, 035409 (2020).

[29] A. Kormányos, G. Burkard, M. Gmitra, J. Fabian, V. Zólyomi, N. D. Drummond, and V. Falko, k·p theory for two-dimensional transition metal dichalcogenide semiconductors, 2D Mater. **2**, 022001 (2015).

[30] See Supplemental Material at http://link.aps.org/supplemental/10.1103/PhysRevMaterials.8.024005 for layer-resolved band structures calculated for the high symmetry configurations as well as complementary plots of energy landscapes and spin textures of intermediate states for all considered materials.

[31] C. Mera Acosta, L. Yuan, G. M. Dalpian, and A. Zunger, Different shapes of spin textures as a journey through the Brillouin zone, Phys. Rev. B **104**, 104408 (2021).

[32] T. Oguchi and T. Shishidou, The surface Rashba effect: A $k \cdot p$ perturbation approach, J. Phys.: Condens. Matter **21**, 092001 (2009).

[33] Z. Gong, G.-B. Liu, H. Yu, D. Xiao, X. Cui, X. Xu, and W. Yao, Magnetoelectric effects and valley-controlled spin quantum gates in transition metal dichalcogenide bilayers, Nat. Commun. **4**, 2053 (2013).

[34] K. F. Mak, K. L. McGill, J. Park, and P. L. McEuen, The valley Hall effect in MoS_2 transistors, Science **344**, 1489 (2014).

[35] J. Lee, K. F. Mak, and J. Shan, Electrical control of the valley Hall effect in bilayer MoS_2 transistors, Nat. Nanotechnol. **11**, 421 (2016).

[36] Q. Liu, X. Zhang, and A. Zunger, Intrinsic circular polarization in centrosymmetric stacks of transition-metal dichalcogenide compounds, Phys. Rev. Lett. **114**, 087402 (2015).

[37] J. Choi, C. Lane, J.-X. Zhu, and S. A. Crooker, Asymmetric magnetic proximity interactions in $MoSe_2/CrBr_3$ van der Waals heterostructures, Nat. Mater. **22**, 305 (2023).

[38] Y. Su and S.-Z. Lin, Current-induced reversal of anomalous Hall conductance in twisted bilayer graphene, Phys. Rev. Lett. **125**, 226401 (2020).

[39] S. Deb, W. Cao, N. Raab, K. Watanabe, T. Taniguchi, M. Goldstein, L. Kronik, M. Urbakh, O. Hod, and M. Ben Shalom, Cumulative polarization in conductive interfacial ferroelectrics, Nature (London) **612**, 465 (2022).

[40] P. Meng, Y. Wu, R. Bian, E. Pan, B. Dong, X. Zhao, J. Chen, L. Wu, Y. Sun, Q. Fu, Q. Liu, D. Shi, Q. Zhang, Y.-W. Zhang, Z. Liu, and F. Liu, Sliding induced multiple polarization states in two-dimensional ferroelectrics, Nat. Commun. **13**, 7696 (2022).

[41] P. Giannozzi *et al.*, Quantum ESPRESSO: A modular and open-source software project for quantum simulations of materials, J. Phys.: Condens. Matter **21**, 395502 (2009).

[42] P. Giannozzi *et al.*, Advanced capabilities for materials modelling with Quantum ESPRESSO, J. Phys.: Condens. Matter **29**, 465901 (2017).

[43] G. Kresse and J. Furthmüller, Efficiency of ab-initio total energy calculations for metals and semiconductors using a plane-wave basis set, Comput. Mater. Sci. **6**, 15 (1996).

[44] P. E. Blöchl, Projector augmented-wave method, Phys. Rev. B **50**, 17953 (1994).

[45] J. P. Perdew, K. Burke, and M. Ernzerhof, Generalized gradient approximation made simple, Phys. Rev. Lett. **77**, 3865 (1996).

[46] M. Buongiorno Nardelli, F. T. Cerasoli, M. Costa, S. Curtarolo, R. D. Gennaro, M. Fornari, L. Liyanage, A. R. Supka, and H. Wang, PAOFLOW: A utility to construct and operate on ab initio Hamiltonians from the projections of electronic wavefunctions on atomic orbital bases, including characterization of topological materials, Comput. Mater. Sci. **143**, 462 (2018).

[47] F. T. Cerasoli, A. R. Supka, A. Jayaraj, M. Costa, I. Siloi, J. Sławińska, S. Curtarolo, M. Fornari, D. Ceresoli, and M. Buongiorno Nardelli, Advanced modeling of materials with PAOFLOW 2.0: New features and software design, Comput. Mater. Sci. **200**, 110828 (2021).

[48] https://doi.org/10.34894/QYT5KP